Frequency-Domain Photoacoustic Microscopy with Resonant Transducer and Interferometric Modulation for High-reliability sO_2 Imaging

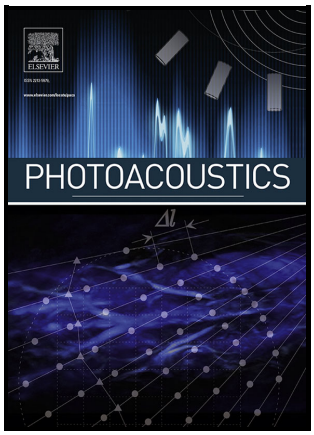

Yong-Jae Lee, Tae Joong Eom, Lihong V. Wang

PII: S2213-5979(26)00040-6

DOI: https://doi.org/10.1016/j.pacs.2026.100834

Reference: PACS100834

To appear in: *Photoacoustics*

Received date: 9 December 2025
Revised date: 14 April 2026
Accepted date: 26 April 2026

Please cite this article as: Yong-Jae Lee, Tae Joong Eom and Lihong V. Wang, Frequency-Domain Photoacoustic Microscopy with Resonant Transducer and Interferometric Modulation for High-reliability sO_2 Imaging, *Photoacoustics,* (2026) doi:https://doi.org/10.1016/j.pacs.2026.100834

Frequency-Domain Photoacoustic Microscopy with Resonant Transducer and Interferometric Modulation for High-reliability sO_2 Imaging

Yong-Jae Lee[1], Tae Joong Eom[1,2*] , and Lihong V. Wang[3*]

Author

[1]Engineering Research Center for Color-modulated Extra-sensory Perception Technology, Pusan National University, Busan 46241, Republic of Korea.

[2]Department of Cogno-Mechatronics Engineering & Optics and Mechatronics Engineering, Pusan National University, Busan 46241, Republic of Korea.

email: eomtj@pusan.ac.kr

[3]Caltech Optical Imaging Laboratory, Andrew and Peggy Cherng Department of Medical Engineering, Department of Electrical Engineering, California Institute of Technology, Pasadena, CA, USA

email: lihong@caltech.edu

*These authors contributed equally as co-corresponding authors.

Abstract

Frequency-domain photoacoustic microscopy (FD-PAM) could leverage a high-Q resonant ultrasound transducer to suppress out-of-band noise and lower the noise-equivalent pressure (NEP) for truly simultaneous multi-wavelength functional imaging. In practice, however, conventional continuous-wave direct modulation makes it difficult to stay within the narrow resonance, leading most implementations to rely on low-Q broadband detectors instead. To obtain accurate and stable hemoglobin oxygen saturation (sO_2) measurements, we implement an acousto-optic modulator (AOM)-based interferometric modulation scheme in FD-PAM, enabling the practical use of a high-Q resonant ultrasound transducer while preserving truly simultaneous dual-wavelength excitation. FD-PAM with interferometric modulation operates robustly within the narrow bandwidth of the high-Q transducer and supports clean spectral separation (SSIM = 0.97 between frequency-separated channels), as well as quantitative sO_2 estimation with <2% within-group variation across oxygenated, mixed, and deoxygenated conditions. We anticipate that this approach will be useful for monitoring drug-induced changes in hemoglobin oxygen saturation and quantitatively evaluating therapeutic response.

Keywords:

frequency domain photoacoustic microscopy, High Q-factor ultrasound transducer, interferometric modulation

1. Introduction

Photoacoustic (PA) imaging is a hybrid modality in which pulsed or intensity-modulated light generates ultrasound within biological tissue via thermoelastic expansion. Leveraging wavelength-dependent absorption and spectroscopic analysis[1–4], PA provides structural and functional measurements (e.g., sO_2, total hemoglobin, lipids, melanin, blood flow, fibrosis)[5–11] and has been broadly applied in ophthalmology, dermatology, neurology, oncology, and cardiology[12–16]. Conventional time-domain photoacoustic imaging and microscopy remain the dominant implementations in the field and continue to advance rapidly through improvements in imaging speed, system performance, and biomedical/clinical applications[17–21]. However, quantitative sO_2 imaging is often limited by temporal interleaving between wavelengths, which degrades spatiotemporal correspondence, and can be further affected by pulse-to-pulse energy variability in pumped solid-state pulsed sources, ultimately reducing functional accuracy.

In contrast, frequency-domain PAM (FD-PAM) inherently supports truly simultaneous multi-wavelength excitation without temporal interleaving, preserving spatiotemporal correlation and enabling precise functional quantification (e.g., sO_2)[22,23]. Moreover, CW-based modulation generates tone-like narrowband photoacoustic responses that can be efficiently extracted by frequency-selective demodulation, providing strong rejection of out-of-band noise[24]. In conventional FD-PAM, a function generator is commonly used to directly modulate the CW excitation intensity via laser current injection, and the resulting acoustic tone is recovered by phase-sensitive detection (e.g., lock-in amplifiers or I/Q demodulation), which enables robust amplitude/phase readout with an effectively narrowed detection bandwidth [25–27]. This direct-modulation scheme is limited by restricted modulation depth, imprecise frequency placement for narrowband detection, and bias-point/amplitude drift, while large-signal injection further causes harmonic distortion and nonlinear dynamics that degrade the linear modulation range and tone purity[28–30]. In principle, employing a high-Q resonant ultrasound transducer in FD-PAM would concentrate detection within a very narrow passband, enhancing sensitivity and lowering the effective noise-equivalent pressure (NEP)[31], yet accurately placing and maintaining the modulation within such a bandwidth is difficult and has remained a practical challenge.

Here we report an FD-PAM system that, by using a high-Q resonant ultrasound transducer, enables reliable, high-precision functional imaging. To accommodate the high-Q transducer, we introduce the interferometric modulation scheme with two acousto-optic modulators (AOM). This approach precisely places distinct beat frequencies for two excitation wavelengths within the transducer's narrow passband, and its near-unity modulation depth increases the modulated optical-intensity component, improving image contrast while mitigating the impact of amplitude noise. We validate the system on representative phantoms and blood samples, demonstrating narrowband resonant operation and compatibility with truly simultaneous multi-wavelength acquisition without temporal interleaving.

2. Methods

2.1 FD-PAM system employing interferometric modulation with high-Q resonant ultrasound transducer

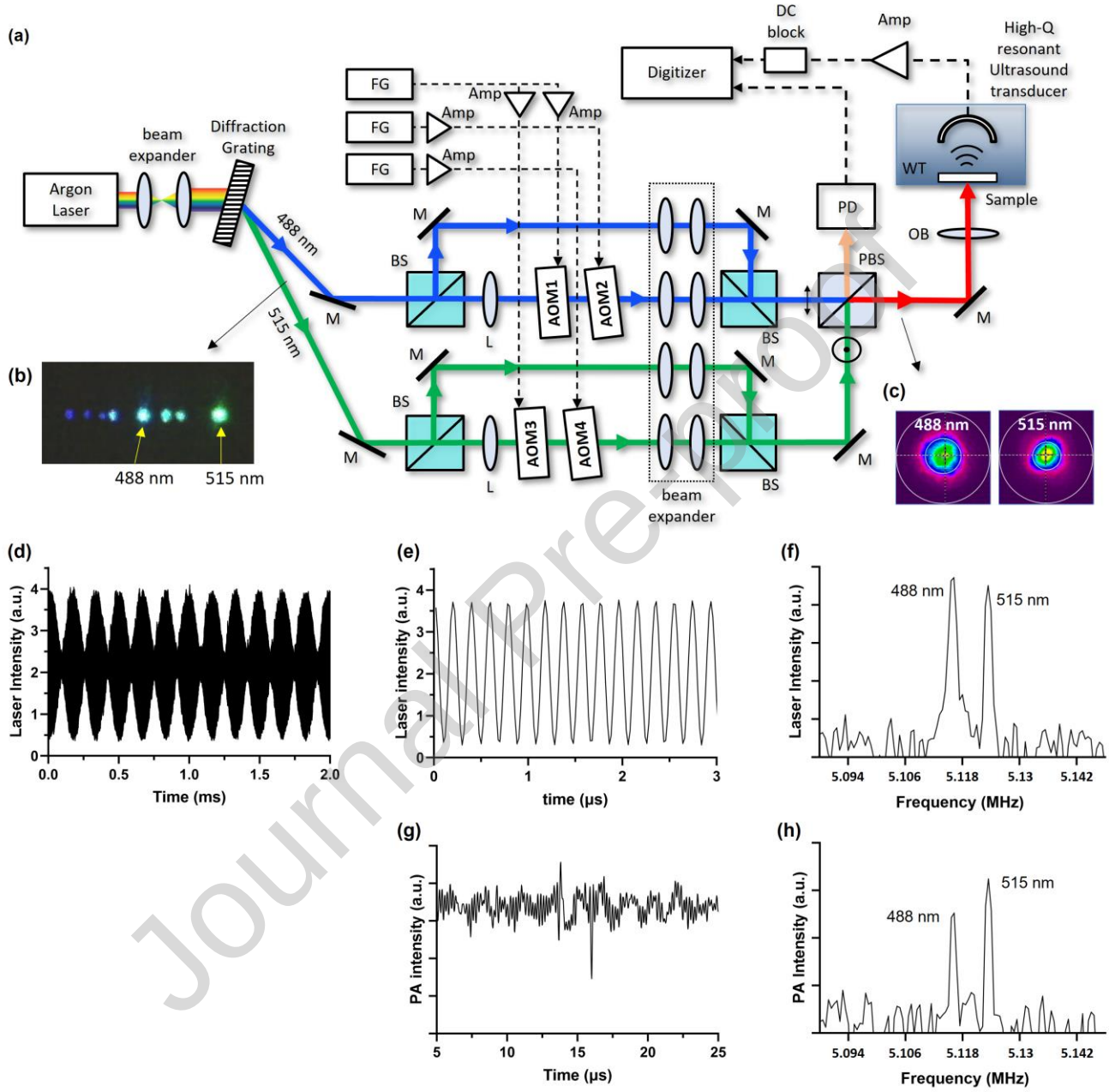

Figure 1. High-sensitivity frequency-domain photoacoustic microscopy (FD-PAM) with interferometric sinusoidal modulation. (a) Optical layout employing an interferometric modulation scheme with two acousto-optic modulators (AOM) and a high-Q resonant ultrasound transducer. (b) Diffraction pattern after the grating, showing spatial separation of the 488 nm and 515 nm lines. (c) Measured beam profiles after the PBS, demonstrating collimated, size-matched beams at both wavelengths. (d) Temporal waveform of the interferometrically modulated 488 nm and 515 nm beams measured by the photodetector. (e) Magnified view of the waveform in (d), highlighting the sinusoidal intensity modulation in the microsecond time scale. (f) Fourier transform of (d), showing two distinct modulation peaks at the assigned beat frequencies. (g) Representative

raw photoacoustic (PA) signal of blood sample recorded with the high-Q resonant ultrasound transducer. (h) Fourier transform of the photoacoustic signal recorded with the high-Q resonant transducer, demonstrating precise detection of the dual-wavelength–modulated components. Abbreviations: BS, beam splitter; FG, function generator; M, mirror; L, lens; PBS, polarization beam splitter; PD, photodetector; OB, objective lens; WT, water tank; Amp, RF amplifier.

Figure 1(a) depicts the FD-PAM setup. A continuous-wave argon-ion laser provides strong emission lines at 488 nm and 515 nm, which are spatially separated by a diffraction grating (Fig. 1(b)) and selected for dual-wavelength sO_2 imaging near the hemoglobin isosbestic region.

For each wavelength, the beam is split by a beam splitter into two arms; one arm is frequency-shifted using a cascaded acousto-optic modulator (AOM) pair and then recombined with the unshifted arm to generate a stable beat signal via interferometric intensity modulation. The beat frequencies are set to $\Delta f \approx 5.115$ MHz (488 nm) and 5.123 MHz (515 nm) by the cascaded AOM configuration (+1st order followed by −1st order), as detailed in Sec. 4.2. Beam expanders homogenize the beam profiles and provide size-matched beams to ensure stable interference and an identical beam waist at the sample (Fig. 1(c)). The wavelength-tagged beams are combined at a polarization beam splitter (PBS) and delivered to the sample to generate photoacoustic (PA) signals. A fraction of the excitation light is monitored by a reference photodetector (PD) to estimate the sample-side fluence (see Sec. 4.3 for calibration and wavelength-dependent detector compensation).

The temporal waveform measured by the PD exhibits sinusoidal intensity modulation for both wavelengths, allowing verification of the modulation depth as well as the 8 kHz frequency separation between the two modulation tones (Fig. 1(d)). Figure 1(e) shows a zoomed-in view of Fig. 1(d), clearly visualizing the microsecond-scale sinusoidal modulation. The Fourier transform of the PD signal reveals two distinct peaks corresponding to the assigned modulation frequencies for the 488 nm and 515 nm channels (Fig. 1(f)); a theoretical description of the modulation scheme is provided in Sec. 2.2.

The photoacoustic signals are detected using a high-Q resonant ultrasound transducer, which was a custom-built piezoceramic bowl transducer. When the two modulated beams are focused onto the sample located at the focal point of the transducer, a representative raw PA waveform of blood sample is obtained (Fig. 1(g)). Its Fourier spectrum (Fig. 1(h)) shows two resolvable frequency-tagged components at the assigned beat frequencies, confirming that both tones lie within the narrow resonant bandwidth (<100 kHz) of the transducer while remaining separable due to the 8 kHz spacing. The isolated frequency-tagged components are then used to reconstruct the dual-wavelength PA signals and compute sO_2.

In summary, high-modulation-depth interferometric excitation enhances PA generation efficiency, while on-resonance narrowband detection with a high-Q resonant transducer suppresses out-of-band noise, enabling high-sensitivity dual-wavelength FD-PAM.

2.2 Analytical comparison of CW laser modulation schemes for FD-PAM

We analytically derive and compare the detected intensity envelopes produced by direct current (DC) modulation and interferometric (beat) modulation. Here, t denotes time (s), f_0 the optical carrier frequency (Hz, ~hundreds of THz), and f_{mod}/ Δf the imposed intensity/beat modulation frequency (Hz, MHz range). The photodetector measures the optical irradiance ($\mathrm{W}\cdot\mathrm{m}^{-2}$) or power (W) averaged over optical cycles; therefore, the experimentally relevant quantity is the envelope $I(t) \propto \langle E^2(t)\rangle$, rather than the optical carrier oscillation at f_0. Throughout this section, $E(t)$denotes the optical electric field at the detector ($\mathrm{V}\cdot\mathrm{m}^{-1}$), while $I(t)$denotes the corresponding time-averaged irradiance ($\mathrm{W}\cdot\mathrm{m}^{-2}$) (equivalently proportional to PD voltage, depending on the readout chain).

To enable a fair comparison—and to reflect CW ANSI/MPE constraints—both modulation schemes are constrained to the same peak irradiance, i.e., $I_{\max}$ is identical in the two cases. Accordingly, all envelopes are peak-normalized such that $\max\{I(t)\} = 1$, isolating the effect of modulation depth and waveform on the spectral component at the modulation frequency.

In direct laser modulation, the optical field is modeled as

$$E_f(t) = E_0\,[1 + m\cos(2\pi f_{\mathrm{mod}} t)]\cos(2\pi f_0 t),$$

where E_0 is the field amplitude ($\mathrm{V}\cdot\mathrm{m}^{-1}$) and $m \in [0,1]$ is the intensity-modulation index (dimensionless). The detected irradiance satisfies $I(t) \propto \langle E^2(t)\rangle$. Averaging over optical cycles yields the intensity envelope,

$$I_f(t) \propto E_0^2\,[1 + m\cos(2\pi f_{\mathrm{mod}} t)].$$

Enforcing equal peak normalization $\max\{I_f(t)\} = I_{\max} = 1$gives

$$I_f^{(\mathrm{peak})}(t) = \frac{1}{1+m}\,[1 + m\cos(2\pi f_{\mathrm{mod}} t)],$$

which spans $I_{\min} = (1-m)/(1+m)$ to $I_{\max} = 1$. In typical direct-modulation implementations using a function generator and current driver, the achievable modulation depth is often limited and remains below unity under practical operating conditions.

In interferometric modulation, two frequency-offset CW fields are interfered (general unequal-amplitude case):

$$E_1(t) = E_{01}\cos(2\pi f_0 t), \qquad E_2(t) = E_{02}\cos(2\pi(f_0 + \Delta f)t),$$

where E_{01}, E_{02} are field amplitudes ($\mathrm{V \cdot m^{-1}}$) and Δf(Hz) is the imposed frequency offset (e.g., set by the AOM drive frequencies). The detected envelope is obtained from $I(t) \propto \langle (E_1 + E_2)^2 \rangle$, yielding

$$I_{\mathrm{het}}(t) \propto I_1 + I_2 + 2\sqrt{I_1 I_2}\cos(2\pi\Delta f\, t),$$

with $I_1 \propto E_{01}^2/2$ and $I_2 \propto E_{02}^2/2$ denoting the time-averaged irradiances of each interfering arm ($\mathrm{W \cdot m^{-2}}$). The corresponding beat modulation depth (visibility) is

$$m_{\mathrm{het}} = \frac{I_{\max} - I_{\min}}{I_{\max} + I_{\min}} = \frac{2\sqrt{I_1 I_2}}{I_1 + I_2},$$

which approaches unity only when the interfering arms are power-balanced ($I_1 = I_2$). The corresponding noiseless time-domain waveforms for the CW outputs, the individual arms after the AOMs (before interference), and the recombined heterodyne signal, together with the dual-tone superposition used in this work, are provided in Supplementary Fig. S1 for clarity.

In our implementation, the photodiode trace in Fig. 1(d) yields $m_{\mathrm{het}} \approx 0.83$ (from measured $I_{\max}$ and $I_{\min}$). We note that m_{het} can be increased toward unity by more closely balancing the interfering arm powers (for each wavelength channel), whereas the present experiments did not explicitly optimize for perfect balance.

2.3 Frequency-domain PA generation model

The absorbed power density (volumetric heating function) in photoacoustics, $H(\mathbf{r}, t)[\mathrm{W/m^3}]$ is written as

$$H(\mathbf{r}, t) = \mu_a(\mathbf{r})\, \Phi(\mathbf{r}, t),$$

where $\mu_a(\mathbf{r})$is the optical absorption coefficient $[\mathrm{m^{-1}}]$ and $\Phi(\mathbf{r}, t)$ is the optical fluence rate (irradiance) $[\mathrm{W/m^2}]$. In our FD scheme, the fluence rate is harmonically modulated as

$$\Phi(\mathbf{r}, t) = \Phi_{DC}(\mathbf{r}) + \Phi_{AC}(\mathbf{r})\cos(\omega t), \omega = 2\pi\Delta f,$$

where $\Delta f$is the modulation (tagging) frequency.

The generated photoacoustic pressure $p(\mathbf{r}, t)$follows the thermoelastic wave equation in the linear regime,

$$\frac{\partial^2 p(\mathbf{r}, t)}{\partial t^2} - c_s^2 \nabla^2 p(\mathbf{r}, t) = \Gamma\, \frac{\partial H(\mathbf{r}, t)}{\partial t},$$

where $c_s$is the speed of sound $[\mathrm{m/s}]$and $\Gamma$is the Grüneisen parameter (dimensionless). Substituting the harmonic heating function yields $\partial H/\,\partial t \propto -\omega\, \mu_a(\mathbf{r})\Phi_{AC}(\mathbf{r})\sin(\omega t)$, indicating that harmonic heating at ωgenerates an acoustic response at the same frequency. Accordingly, the pressure amplitude at ωscales with

$\omega\Gamma\mu_a\Phi_{AC}$, up to acoustic propagation and detection factors.

Thermal diffusion in FD operation can be characterized by the thermal diffusion length

$$\delta_{th} = \sqrt{\frac{2\alpha}{\omega}},$$

where $\alpha$is the thermal diffusivity $[\mathrm{m}^2/\mathrm{s}]$. In FD excitation, thermal confinement can be interpreted by comparing $\delta_{th}$with a characteristic optical/absorber dimension L; localized temperature oscillations are maintained when $\delta_{th} \ll L$, which is increasingly satisfied at MHz-range modulation.

For completeness, the frequency-domain form of the wave equation can be written by expressing the pressure as $p(\mathbf{r},t) = \Re\{\tilde{p}(\mathbf{r},\omega)e^{i\omega t}\}$, yielding a Helmholtz-type equation

$$(\nabla^2+k^2)\tilde{p}(\mathbf{r},\omega) = -\frac{i\omega\Gamma}{c_s^2}\,\tilde{H}(\mathbf{r},\omega), k = \frac{\omega}{c_s},$$

where $\tilde{H}(\mathbf{r},\omega)$is the complex amplitude of the harmonic heating term. This representation makes explicit that the detected signal at the tagging frequency is governed by the product of (i) the harmonic heating strength and (ii) the acoustic propagation and detection transfer functions.

Finally, the measured spectrum is shaped by the frequency response of the high-Q resonant ultrasound transducer (UST), which acts as a narrowband filter. The detected signal can be expressed as

$$S(\omega) = H_{UST}(\omega)\,P(\omega) + N(\omega),$$

where $H_{UST}(\omega)$is the transducer transfer function, $P(\omega)$denotes the acoustic pressure spectrum at the detector, and $N(\omega)$is additive noise. As a result, wavelength-encoded tones that are precisely placed within the narrow UST passband are preferentially detected, enabling robust frequency-tagged demodulation for functional quantification.

2.4 FD-PAM system setup with resonance transducer

The functional FD-PAM imaging system employed a multi-line argon-ion laser (LS200A, Dynamic Laser, USA) as the excitation source. Two output wavelengths—488 nm and 515 nm—were selected using a transmission diffraction grating, with a beam expander installed beforehand to improve diffraction efficiency.

Each wavelength was modulated using a pair of acousto-optic modulators (AOMs; I-M110-2C10B6-3-GH26, G&H, UK). The AOMs were driven by four RF sources, with modulation frequencies tuned to generate beat signals for frequency tagging of each wavelength. The modulated beams were combined and delivered to the sample through a polarizing beam splitter (PBS). A portion of the combined beam was also directed to a photodetector (PD) for real-time fluence monitoring.

Photoacoustic signals were detected using a custom-built piezoceramic bowl transducer (Ferroperm-Piezo, USA). To determine the transducer's resonance frequency in water, the driving frequency of one AOM was tuned while monitoring PA signal amplitude. The peak response was observed at 5.118 MHz, and this value was used to match the beat frequency during imaging. The measured 3-dB bandwidth of the transducer was 100 kHz.

The detected PA signals were amplified in two stages using a 25 dB low-noise amplifier (ZFL-500, Mini-Circuits, USA) and a 40 dB broadband amplifier (ZX60-100VHX+, Mini-Circuits, USA), then digitized using a high-speed acquisition board (ATS9350, AlazarTech, USA). For full-field imaging, a two-axis motorized stage was used to raster-scan the sample. All acquired signals were processed using FFT to extract the amplitude components corresponding to the modulated wavelengths.

2.5 Frequency tagging with cascaded AOMs

We generated a stable beat tone for each wavelength using two acousto-optic modulators (AOMs) arranged in series and operated on opposite diffraction orders, providing precise control of the optical frequency shift while maintaining high interferometric contrast.

AOM1 was aligned to transmit only the +1st-order diffracted beam, imparting a nominal +80.000 MHz shift. The beam then entered AOM2, aligned to the −1st-order path to impart a tunable $-f_{\mathrm{AOM2}}$ shift. The net optical frequency after the pair becomes $f_0 + f_{\mathrm{AOM1}} - f_{\mathrm{AOM2}}$; when interfered with the unshifted arm, the heterodyne beat frequency is

$$\Delta f = |f_{\mathrm{AOM1}} - f_{\mathrm{AOM2}}|.$$

We first swept Δf while monitoring the PA amplitude in water to identify the resonant ultrasound transducer response; the peak occurred at 5.118 MHz with a measured 3-dB bandwidth ≈ 100 kHz. After locating the resonance, we placed the tag frequencies within this passband to maximize sensitivity and minimize detuning-induced roll-off. For dual-wavelength operation, tags were set to 5.115 and 5.123 MHz: the 8 kHz spacing ensures clean FFT separation, while the ±3–5 kHz detuning from the 5.118 MHz center preserves on-resonance sensitivity with negligible amplitude roll-off.

2.6 Laser fluence calibration and wavelength-dependent sensitivity compensation

Accurate hemoglobin oxygen saturation quantification requires reliable normalization of photoacoustic (PA) signals to laser fluence. Since direct laser intensity measurement at the sample is not feasible during imaging, we employed a two-step correction strategy as shown in Fig. 2.

First, to estimate sample-side fluence indirectly, we calibrated the output of a reference photodetector (PD) placed after the PBS against that of a sample-side PD. Due to the absence of separate polarization control for the 488 nm and 515 nm beams, the PBS splitting ratio differed between wavelengths. We corrected this by acquiring PD signals at various power levels, extracting modulation amplitudes via FFT, and applying linear fitting. The calibrated reference PD output closely predicted sample-side fluence (Fig. 2a,b).

Second, we compensated for the wavelength dependence of photodiode's responsivity. Even after fluence calibration, differences in spectral responsivity caused discrepancies in how optical power was converted to electrical signal. To address this, we normalized the PD-derived laser intensity by the corresponding PA signal, revealing a lower effective sensitivity at 488 nm. Applying the earlier calibration factor corrected this mismatch and aligned the 488 nm response with that of 515 nm (Fig. 2c).

This two-step procedure enabled accurate, real-time fluence estimation and consistent normalization across wavelengths, improving the robustness of functional PA measurements.

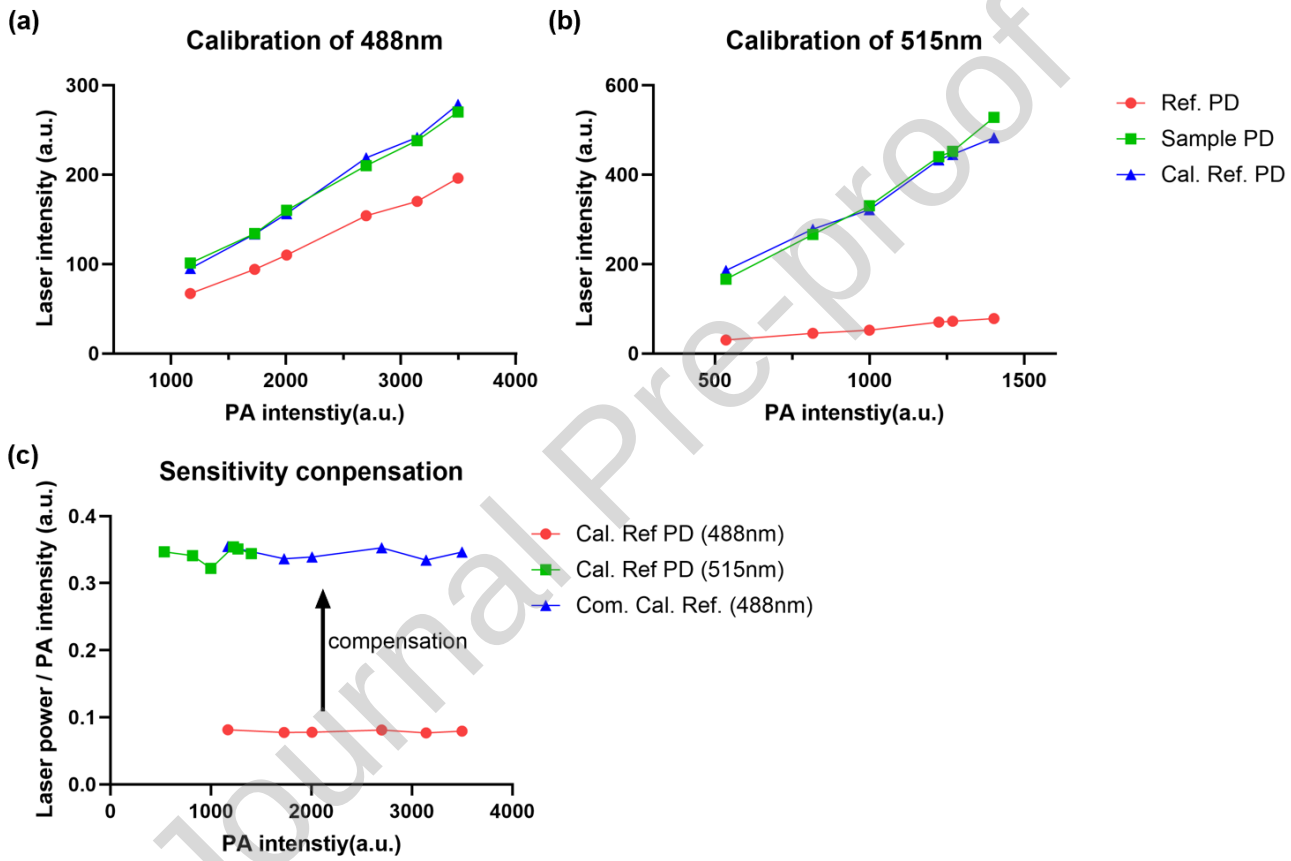

Figure 2. (a, b) PBS-induced splitting ratio calibration for 488 nm and 515 nm wavelengths, respectively. Reference PD readings were linearly fitted to sample PD measurements and used to generate calibrated reference values. (c) Sensitivity compensation across wavelengths. After normalization by PA intensity, wavelength-dependent variation was corrected using the calibrated fluence data.

2.7 Oxygen saturation sample

To evaluate the performance of the FD-PAM system in oxygen saturation estimation, blood samples with controlled oxygenation levels were prepared. Blood samples were de-identified and research-use-only materials. The samples were divided into three groups: oxygenated, deoxygenated, and a 1:1 volume mixture.

Oxygenated blood was prepared by exposing the sample to pure oxygen gas until the saturation level stabilized near 100%. Deoxygenated blood was obtained by bubbling carbon dioxide gas through the sample until a

minimal oxygen saturation level was reached. The mixed sample was created by combining equal volumes of the oxygenated and deoxygenated samples.

To minimize optical and acoustic interference from white blood cells, they were removed via centrifugation, ensuring that the resulting photoacoustic signal originated primarily from hemoglobin. Each sample was placed in a transparent capillary tube and sealed to prevent gas exchange with the environment. The capillaries were submerged in a water bath to ensure efficient acoustic coupling with the ultrasound transducer. Imaging was then performed using the FD-PAM system at the two selected wavelengths (488 nm and 515 nm), chosen for their differential absorption by oxyhemoglobin and deoxyhemoglobin.

3. Results

3.1 Spectral decomposition and image fidelity verification using black hair

We evaluated frequency-based spectral decomposition using a black human hair phantom (Fig. 3(a)). Photoacoustic (PA) waveforms were demodulated in the frequency domain (FFT) at the assigned beat frequencies to yield two images, each corresponding to one modulated wavelength (Fig. 3(b),(c)).

To assess spatial fidelity between the simultaneously acquired wavelength-tagged images, we computed the structural similarity index (SSIM). A fixed intensity threshold was applied beforehand to suppress background and restrict the comparison to relevant high-intensity PA regions.

The measured SSIM of 0.97 (Fig. 3(d)) indicates excellent geometric and morphological agreement between the two frequency-separated images, confirming that frequency tagging preserves spatial integrity and does not introduce misregistration or distortion. This property is critical for functional imaging, where pixel-wise spectral analysis (e.g., sO_2 mapping) requires precise spatial correspondence across wavelengths.

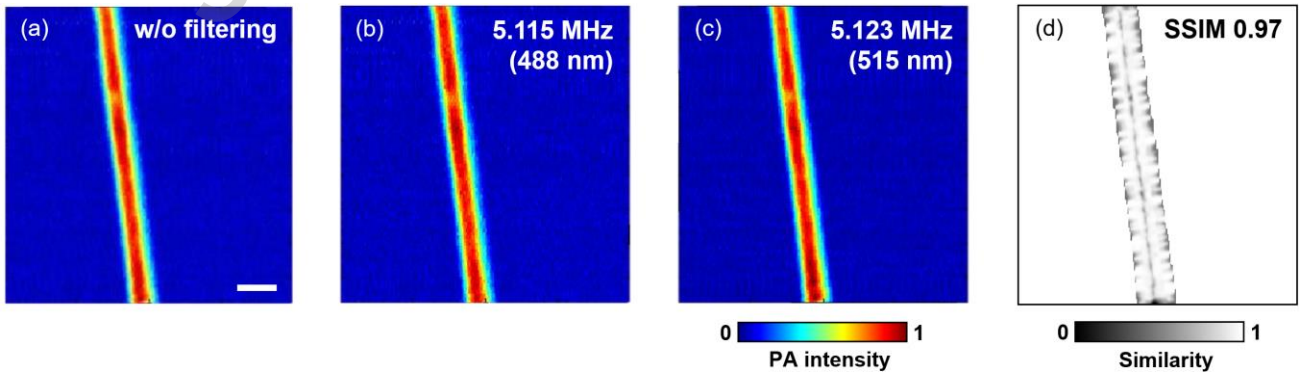

Figure 3. Frequency-based separation of photoacoustic images and structural similarity analysis. (a) PA image of black hair without frequency filtering. (b,c) Frequency-separated photoacoustic image at 5.115 MHz (488 nm excitation) and 5.123 MHz (515 nm excitation), respectively. (d) SSIM map comparing the images in (b) and (c).

Scale bar: 200 μm.

3.2 Oxygen saturation estimation

We assessed the accuracy and consistency of oxygen-saturation (sO_2) estimation using prepared blood samples at three oxygenation states—oxygenated (Oxy), mixed (1:1 Oxy:Deoxy), and deoxygenated (Deoxy)—as shown in Fig. 4(a). For each strip, five 5 × 5-pixel ROIs were manually selected along the vertical direction (positions 1–5 from top to bottom; dashed boxes) to compute the mean and standard deviation of sO_2.

Frequency-tagged reconstruction yielded well-separated sO_2 levels across the three groups (Fig. 4(b)): Oxy, 97.8% ± 1.74%; 1:1 mixed, 51.5% ± 1.34%; and Deoxy, 6.19% ± 1.23% (mean ± s.d., n = 5 ROIs per group, each 5 × 5 pixels). The low within-group variation indicates stable quantification and high spatial fidelity between the simultaneously acquired wavelength channels.

These results confirm that the proposed FD-PAM system accurately discriminates multiple hemoglobin oxygenation levels over a physiologically relevant range. We note that the scans used a servo-driven mechanical stage rather than a high-speed scanner (galvo/MEMS); the reduced temporal correlation between adjacent ROIs within the same strip may modestly contribute to the observed variance.

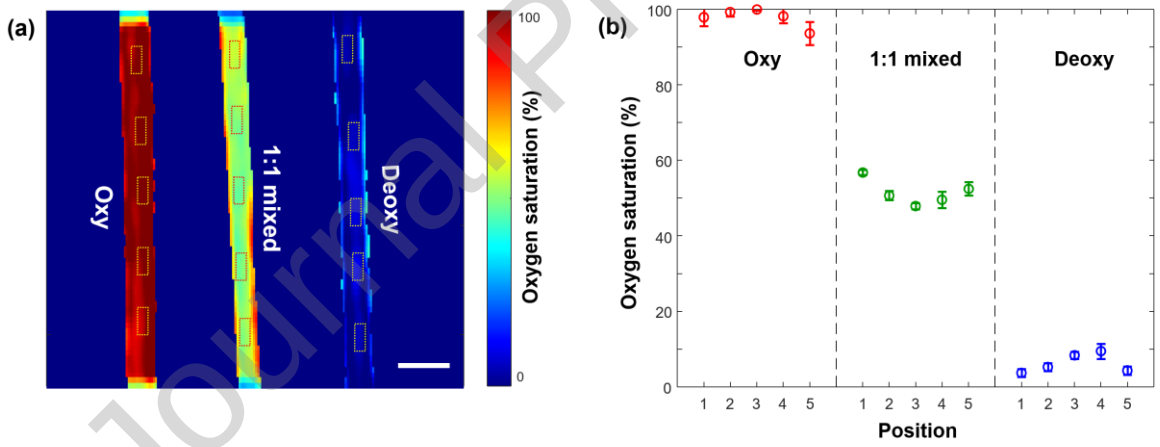

Figure 4. sO_2 PA image and corresponding oxygen saturation analysis. (a) Photoacoustic image of oxygen saturation (sO_2) in blood samples with three different oxygenation states: Oxy, mixed (1:1), and Deoxy. (b) Bar plot showing oxygen saturation values across five ROIs per blood sample, confirming distinct sO_2 levels with low within-group variability. Scale bar: 200 μm.

4. Discussion

To obtain more reliable functional information, we implemented an interferometric modulation scheme in FD-PAM to enable the use of a high-Q resonant transducer. The AOM-based interferometer provides full-depth sinusoidal intensity modulation and precisely places two distinct modulation frequencies within the transducer's narrow receive bandwidth (< 100 kHz). This architecture supports simultaneous multi-wavelength excitation without temporal multiplexing, enabling stable quantification and high spatial fidelity between the simultaneously acquired wavelength channels.

Spectral separation was verified with a black hair phantom: the two wavelength-tagged PA channels were cleanly decomposed, and an SSIM of 0.97 confirmed that spatial and morphological information was preserved. For sO_2 estimation, the system clearly separated oxygenated, mixed, and deoxygenated blood samples with low within-group variation; across five regions of interest (each 5 × 5 pixels), the mean within-ROI standard deviation did not exceed 1.74%, indicating stable, reproducible quantification under simultaneous dual-wavelength operation.

Compared with conventional time-domain PAM (TD-PAM), which uses pulsed excitation and broadband ultrasonic detection to enable time-of-flight–based depth gating, our implementation employs a resonant high-Q transducer operated at a specific narrowband frequency. Because the measurement is intentionally confined to a narrow frequency band and does not rely on time-of-flight reconstruction, it does not provide axial sectioning (depth gating). Accordingly, it is not intended for general depth-resolved imaging, but rather for en-face functional mapping in targets where the most informative contrast is inherently surface-weighted. In many practical scenarios, the effective optical penetration depth is limited and functional readouts are dominated by superficial vasculature or near-surface composition, such that surface-weighted measurements can still provide actionable information. For example, in cardiovascular assessment, identifying the presence and spatial distribution of lipid-rich components near the luminal surface of plaques is clinically relevant even without full depth discrimination, and repeated en-face mapping at a consistent plane can be prioritized for longitudinal monitoring. Overall, the high-Q strategy is chosen to maximize frequency specificity and sensitivity and to suppress out-of-band noise, thereby improving the robustness and repeatability of functional quantification in these surface-weighted use cases.

Several practical constraints remain. Although prior FD-PAM studies have demonstrated in vivo imaging, the present prototype was designed primarily to validate the signal-formation principle of simultaneous dual-tone excitation with high-Q narrowband detection rather than to serve as a fully optimized in vivo platform. In its current form, the transmission-type geometry and servo-driven raster scanning make in vivo imaging impractical due to limited accessibility and animal positioning constraints and increased susceptibility to motion artifacts from respiration and heartbeat, which can compromise quantitative sO_2 mapping. Future implementations will address these limitations by transitioning to a reflection-mode configuration and adopting faster beam scanning such as galvanometric or MEMS scanners to increase throughput and improve temporal consistency.

More broadly, the proposed scheme is not limited to an argon-ion laser and, in principle, should be compatible with compact CW diode lasers or fiber lasers, provided that sufficient optical power and coherence are available to sustain stable self-heterodyne interference and that the frequency control is stable enough to place the modulation tones within the high-Q transducer passband. Compared with the current argon-laser-based free-space setup, diode or fiber laser sources could simplify operation and packaging and may offer improved long-term stability in practical systems [32].

In summary, we enable FD-PAM to use a high-Q transducer by introducing a two-AOM interferometric modulation scheme that precisely places each beat frequency within the narrow passband and achieves near-unity modulation depth. Looking ahead, we expect that this approach could play an important role in precisely monitoring drug-induced changes in hemoglobin oxygen saturation, thereby supporting quantitative evaluation of therapeutic response.

References

[1] M. Xu, L. V. Wang, Photoacoustic imaging in biomedicine, Review of Scientific Instruments 77(4) (2006) 1–22. https://doi.org/10.1063/1.2195024.

[2] S. Jeon, J. Kim, D. Lee, J.W. Baik, C. Kim, Review on practical photoacoustic microscopy, Photoacoustics 15 (2019) 100141. https://doi.org/10.1016/j.pacs.2019.100141.

[3] B. Cox, J.G. Laufer, S.R. Arridge, P.C. Beard, Quantitative spectroscopic photoacoustic imaging: a review, J. Biomed. Opt. 17(6) (2012) 061202. https://doi.org/10.1117/1.JBO.17.6.061202.

[4] C. Liu, L. Wang, Functional photoacoustic microscopy of hemodynamics: a review, Biomed. Eng. Lett. 12 (2022) 97–124. https://doi.org/10.1007/s13534-022-00220-4.

[5] S. Hu, K.I. Maslov, V. Tsytsarev, L. V. Wang, Functional transcranial brain imaging by optical-resolution photoacoustic microscopy, J. Biomed. Opt. 14(4) (2009). https://doi.org/10.1117/1.3194136.

[6] S. Hu, K. Maslov, L. V. Wang, Second-generation optical-resolution photoacoustic microscopy with improved sensitivity and speed, Opt. Lett. 36(7) (2011) 1134. https://doi.org/10.1364/OL.36.001134.

[7] K. Jansen, M. Wu, A.F.W. van der Steen, G. van Soest, Lipid detection in atherosclerotic human coronaries by spectroscopic intravascular photoacoustic imaging, Opt. Express 21(18) (2013) 21472. https://doi.org/10.1364/OE.21.021472.

[8] T.T. Mai, S.W. Yoo, S. Park, J.Y. Kim, K.H. Choi, C. Kim, S.Y. Kwon, J.J. Min, C. Lee, In vivo quantitative vasculature segmentation and assessment for photodynamic therapy process monitoring using photoacoustic microscopy, Sensors 21(5) (2021) 1–15. https://doi.org/10.3390/s21051776.

[9] J. Yao, K.I. Maslov, Y. Shi, L.A. Taber, L. V Wang, In vivo photoacoustic imaging of transverse blood flow by using Doppler broadening of bandwidth, Opt. Lett. 35(9) 2010. https://doi.org/10.1364/OL.35.001419.

[10] E. Park, Y.-J. Lee, C. Lee, T.J. Eom, Effective photoacoustic absorption spectrum for collagen-based tissue imaging, J. Biomed. Opt. 25(5) (2020) 1. https://doi.org/10.1117/1.jbo.25.5.056002.

[11] E. Park, Y.J. Lee, C. Kim, T.J. Eom, Azimuth mapping of fibrous tissue in linear dichroism-sensitive photoacoustic microscopy, Photoacoustics 31 (2023). https://doi.org/10.1016/j.pacs.2023.100510.

[12] Z. Hosseinaee, Nima Abbasi, N. Pellegrino, L. Khalili, L. Mukhangaliyeva, P. Haji Reza, Functional and structural ophthalmic imaging using noncontact multimodal photoacoustic remote sensing microscopy and optical coherence tomography, Sci. Rep. 11 (2021). https://doi.org/10.1038/s41598-021-90776-5.

[13] Y. Ying, H. Zhang, L. Lin, Photoacoustic Imaging of Human Skin for Accurate Diagnosis and Treatment Guidance, Optics 5(1) (2024) 133–150. https://doi.org/10.3390/opt5010010.

[14] S.V. Bodea, G.G. Westmeyer, Photoacoustic Neuroimaging - Perspectives on a Maturing Imaging Technique and its Applications in Neuroscience, Front. Neurosci. 15 (2021). https://doi.org/10.3389/fnins.2021.655247.

[15] T.L. Lefebvre, E. Brown, L. Hacker, T. Else, M.E. Oraiopoulou, M.R. Tomaszewski, R. Jena, S.E. Bohndiek, The Potential of Photoacoustic Imaging in Radiation Oncology, Front. Oncol. 12 (2022).

https://doi.org/10.3389/fonc.2022.803777.

[16] A. Karlas, N.A. Fasoula, K. Paul-Yuan, J. Reber, M. Kallmayer, D. Bozhko, M. Seeger, H.H. Eckstein, M. Wildgruber, V. Ntziachristos, Cardiovascular optoacoustics: From mice to men – A review, Photoacoustics 14 (2019) 19–30. https://doi.org/10.1016/j.pacs.2019.03.001.

[17] T.W. Murray, O. Balogun, High-sensitivity laser-based acoustic microscopy using a modulated excitation source, Appl. Phys. Lett. 85(14) (2004) 2974–2976. https://doi.org/10.1063/1.1802387.

[18] E. Park, D. Kim, M. Ha, D. Kim, C. Kim, A comprehensive review of high-performance photoacoustic microscopy systems, Photoacoustics 44 (2025). https://doi.org/10.1016/j.pacs.2025.100739.

[19] X. Zhu, L. Menozzi, S.W. Cho, J. Yao, High speed innovations in photoacoustic microscopy, NPJ Imaging 2 (2024). https://doi.org/10.1038/s44303-024-00052-0.

[20] F. Knieling, S. Lee, V. Ntziachristos, A primer on current status and future opportunities of clinical optoacoustic imaging, NPJ Imaging 3 (2025). https://doi.org/10.1038/s44303-024-00065-9.

[21] S. Contador, Á. Jiménez, E. Lage, C. López, J. Aguirre, An Ultra-Low-Cost Optoacoustic Method for Imaging Specific Biological Structures, Diagnostics 16 (2026). https://doi.org/10.3390/diagnostics16030436.

[22] B. Lashkari, S.S. Sean Choi, M.E. Khosroshahi, E. Dovlo, A. Mandelis, Simultaneous dual-wavelength photoacoustic radar imaging using waveform engineering with mismatched frequency modulated excitation, Opt. Lett. 40(7) (2015) 1145. https://doi.org/10.1364/ol.40.001145.

[23] G. Langer, B. Buchegger, J. Jacak, T.A. Klar, T. Berer, Frequency domain photoacoustic and fluorescence microscopy, Biomed. Opt. Express 7(7) (2016) 2692. https://doi.org/10.1364/boe.7.002692.

[24] D. George, H. Lloyd, R.H. Silverman, P. V. Chitnis, A frequency-domain non-contact photoacoustic microscope based on an adaptive interferometer, J. Biophotonics 11(6) (2018). https://doi.org/10.1002/jbio.201700278.

[25] G.J. Tserevelakis, E. Tekonaki, M. Kalogeridi, I. Liaskas, A. Pavlopoulos, G. Zacharakis, Hybrid Fluorescence and Frequency-Domain Photoacoustic Microscopy for Imaging Development of Parhyale hawaiensis Embryos, Photonics 10 (2023). https://doi.org/10.3390/photonics10030264.

[26] S. Kellnberger, D. Soliman, G.J. Tserevelakis, M. Seeger, H. Yang, A. Karlas, L. Prade, M. Omar, V. Ntziachristos, Optoacoustic microscopy at multiple discrete frequencies, Light Sci. Appl. 7 (2018). https://doi.org/10.1038/s41377-018-0101-2.

[27] K. Maslov, L. V. Wang, Photoacoustic imaging of biological tissue with intensity-modulated continuous-wave laser, J. Biomed. Opt. 13(2) (2008) 024006. https://doi.org/10.1117/1.2904965.

[28] Y. Fan, A. Mandelis, G. Spirou, I. Alex Vitkin, Development of a laser photothermoacoustic frequency-swept system for subsurface imaging: Theory and experiment, J. Acoust. Soc. Am. 116(6) (2004) 3523–3533. https://doi.org/10.1121/1.1819393.

[29] M. Ahmed, G. Abdullah, A. Mahmoud, Exploring High-Order Distortions Associated with Directly

Modulated Laser Diodes in Analog Optical Fiber Systems: The Role of Modulation Depth and Fiber Length, LIRA 1(2) (2025). https://lira.journals.ekb.eg/.

[30] J. Lu, S. Sun, X. Guo, Research on high frequency direct modulation of laser light source, in: Phys. Procedia 19(2011) 442–446. https://doi.org/10.1016/j.phpro.2011.06.190.

[31] A.M. Winkler, K. Maslov, L. V. Wang, Noise-equivalent sensitivity of photoacoustics, J. Biomed. Opt. 18(9) (2013) 097003. https://doi.org/10.1117/1.jbo.18.9.097003.

[32] M. Seeger, A. Stylogiannis, L. Prade, S. Glasl, V. Ntziachristos, Overdriven laser diode optoacoustic microscopy, Sci. Rep. 13 (2023). https://doi.org/10.1038/s41598-023-46855-w.

Yong-Jae Lee received his Ph.D. degree in Physics from Chungnam National University, Daejeon, Republic of Korea. He is currently post-doctoral research Professor of Engineering Research Center for Color-Modulated Extra-Sensory Perception Technology at Pusan National University in Republic of Korea. His research interests are the development of photoacoustic imaging system, high energy wavelength tunable laser, polarization-sensitive optical coherence tomography.

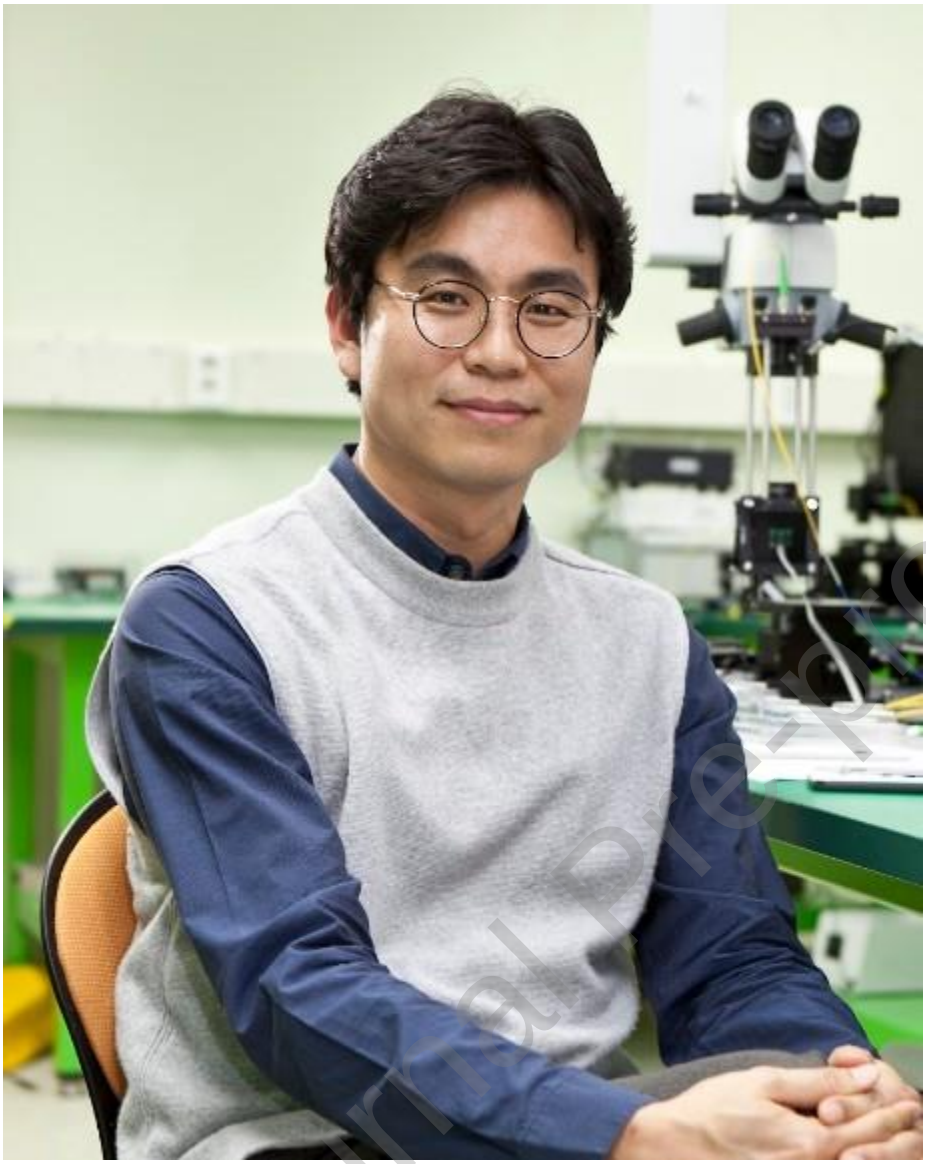

Tae Joong Eom received his Ph.D. degree in Electronics from Gwangju Institute of Science and Technology, Gwangju, Republic of Korea. He is currently an Assistant professor in the Department of Optics and Mechatronics Engineering at Pusan National University in the Republic of Korea. His research interests are the development of novel biomedical imaging techniques, including clinical optical coherence tomography and label-free photoacoustic microscopy tomography.

Lihong V. Wang is Bren Professor of Medical and Electrical Engineering at Caltech. Published 580 journal articles (h-index = 167, citations = 121,000). Delivered 580 keynote/plenary/ invited talks. Published the first functional photoacoustic CT, 3D photoacoustic microscopy, and compressed ultrafast photography (world's fastest camera). Served as Editor-inChief of the Journal of Biomedical Optics. Received the Goodman Book

Award, NIH Outstanding Investigator and Director's Pioneer Awards, OSA Mees Medal, IEEE Technical Achievement and Biomedical Engineering Awards, SPIE Chance Award, IPPA Senior Prize, OSA Feld Biophotonics Award, and an honorary doctorate from Lund University, Sweden. Inducted into the National Academy of Engineering.

CRediT authorship contribution statement

Y.-J.L.: Conceptualization, Formal analysis, Data curation, Methodology. **T.J.E.**: Data curation, Funding acquisition, Project administration, Resources, Supervision. **L.W.**: Funding acquisition, Resources, Supervision. All authors discussed the results and contributed to the writing.

Declaration of Competing Interest

L.V.W. has a financial interest in Microphotoacoustics, Inc., CalPACT, LLC, and Union Photoacoustic Technologies, Ltd., which, however, did not support this work. The other authors declare no competing interests.

Acknowledgments

This work was supported in part by the National Research Foundation of Korea (NRF) under Grants NRF-RS-2021-NR060086 and NRF-RS-2023-00223764, by the Technology Development Program (RS-2023-00304976) funded by the Ministry of SMEs and Startups (MSS, Korea), and by the Korea Institute for Advancement of Technology (KIAT) under Grant RS-2024-00411221. It was also supported by the National Institutes of Health (U01 EB029823 [BRAIN Initiative], R35 CA220436 [Outstanding Investigator Award], and R01 CA282505) and by grant 2024-337784 from the Chan Zuckerberg Initiative DAF, an advised fund of the Silicon Valley Community Foundation.

Appendix A. Supplementary material

Supplementary material

Data availability

The raw data underlying Fig. 1(g) and the corresponding FFT/source data for Fig. 1(h) are publicly available at Zenodo https://zenodo.org/records/19453671. Additional data are available from the corresponding author upon reasonable request.

Declaration of Competing Interest

☒ The authors declare that they have no known competing financial interests or personal relationships that could have appeared to influence the work reported in this paper.

☐ The authors declare the following financial interests/personal relationships which may be considered as potential competing interests: